Quaternary Research (2017), **88**, 71–88.

doi:10.1017/qua.2017.23

Paleoflood records from sinkholes using an example from the Ebro River floodplain, northeastern Spain

Francisco Gutiérrez[a]*, Mario Zarroca[b], Carmen Castañeda[c], Domingo Carbonel[a], Jesús Guerrero[a], Rogelio Linares[b], Carles Roqué[d], Pedro Lucha[e]

[a]Departamento de Ciencias de la Tierra, Universidad de Zaragoza, C/. Pedro Cerbuna 12, 50009 Zaragoza, Spain
[b]Departamento de Geología, Universidad Autónoma de Barcelona, E-08193 Barcelona, Spain
[c]Estación Experimental de Aula Dei, EEAD-CSIC, Av. Montañana 1001, 50059 Zaragoza, Spain
[d]Àrea de Geodinàmica Externa i Geomorfologia, Universitat de Girona, Campus Montilivi, E-17071 Girona, Spain
[e]Departamento de Didáctica de las Ciencias Experimentales, Universidad de Zaragoza, C/. Pedro Cerbuna 12, 50009 Zaragoza, Spain

(Received September 15, 2016; Accepted February 10, 2017)

Abstract

This work introduces for the first time the concept of using sinkholes in fluvial valleys as recorders of past floods. The notion is illustrated through the investigation of a complex sinkhole located in a broad floodplain underlain by salt-bearing Cenozoic evaporites. This active sinkhole comprises a large subsidence depression affecting the floodplain and the edge of a terrace, and a nested collapse sinkhole that used to host a sinkhole pond. A borehole drilled in the buried sinkhole pond revealed an ~7.8-m-thick fill that records around 2700 yr of clayey lacustrine deposition interrupted by three types of detrital facies. Two thick pebble gravel beds have been attributed to major high-competence floods: a paleoflood that occurred in Visigothic times (1537–1311 cal yr BP) and the 1961 Great Ebro River Flood, which is the largest event of the instrumental record. A trench dug in the portion of the terrace affected by subsidence exposed a mid-Holocene slack-water paleoflood deposit. The disadvantages and advantages of sinkholes as archives of past flood histories are discussed.

Keywords: Paleohydrology; Sinkhole lakes; Evaporite karst; Subsidence rate; Trenching

INTRODUCTION

Traditional flood-frequency analyses are based on gauging records that cover short time spans and historical data with limited accuracy. Moreover, the operation of gauging stations frequently fails during the most important events: extremely large and rare floods. Consequently, the hazard estimates for large and long return period floods, derived from extrapolations, have a questionable reliability. The magnitude and frequency relationships of large floods are essential for flood risk management (e.g., definition of the flooding zone) and the design or retrofitting of costly engineering structures (e.g., large dams and nuclear facilities). These limitations can be partially overcome by conducting paleoflood hydrologic studies, which provide information on the magnitude and chronology of large floods using geologic evidence (Kochel and Baker, 1982; Baker, 2003). Paleoflood data allow for expanding the temporal length of flood catalogs and reduce the uncertainty in estimates of long return period floods (e.g., Benito et al., 2004). Past floods may be recorded as erosional and depositional features formed near maximum water levels, notably slack-water deposits. The latter are fine-grained sediments that accumulate from sediment-laden floodwaters at high localities, where the flow becomes separated from the main tread of flood flow, and can be used as paleostage indicators (Baker, 1987; Kochel and Baker, 1988; Baker et al., 2002). They are most frequent in deep and narrow bedrock canyons, where floods produce large increases of water stage, and typically form in tributary mouths, in caves or alcoves, in zones of sharp channel widening, and on high terraces (Baker et al., 2002). Moreover, those bedrock channels, characterized by relatively stable boundaries, are the most appropriate for reliably converting floodwater elevations into paleoflood discharge estimates.

Alluvial channels and broad floodplains are commonly inadequate geomorphic settings for finding long and complete geologic records of paleofloods (e.g., Baker, 2003; Benito et al., 2004). However, in valley reaches underlain by

*Corresponding author at: Departamento de Ciencias de la Tierra, Universidad de Zaragoza, C/. Pedro Cerbuna 12, 50009 Zaragoza, Spain. E-mail: fgutier@unizar.es (F. Gutiérrez).

soluble bedrock, the sedimentary fill of sinkhole lakes developed within the floodplain, and low terraces might include valuable archives of past floods.

Sinkholes are enclosed depressions characteristic of karst regions that may result from the differential corrosional lowering of soluble bedrock (solution sinkholes) or from subsurface dissolution and the subsidence of the overlying sediments (subsidence sinkholes) by different mechanisms (i.e., collapse, sagging, and suffosion) (Gutiérrez, 2016 and references therein). Sinkhole sediments have been investigated for multiple purposes: (1) reconstructing paleoenvironmental and paleoclimatic variability (e.g., Laury, 1980; Whitmore et al., 1996; Hyatt and Gilbert, 2004; Morellón et al., 2009; Barreiro-Lostres et al., 2014); (2) investigating paleontological and archaeological sites (e.g., Carbonell et al., 2008; Calvo et al., 2013; Zaidner et al., 2014; Gutiérrez et al., 2016); (3) estimating erosion rates and their temporal variability in small catchments (e.g., Turnage et al., 1997; Hart, 2014); (4) inferring quantitatively the evolution of the subsidence phenomena using the trenching technique in combination with geochronological data (e.g., Gutiérrez et al., 2009, 2011, 2014; Carbonel et al., 2014, 2015; Gutiérrez, 2016); and (5) identifying the sedimentary signature of hurricanes recorded in bedrock collapse sinkholes, both onshore (cenotes) and offshore (blue holes) (Gischler et al., 2008; Lane et al., 2011; Brown et al., 2014). For example, Brown et al. (2014) recognized two historical hurricanes (1967 Hurricane Beulah and 1991 Hurricane Gilbert) in the sediments of an 80-m-deep sinkhole lake located 10 km inland of the Caribbean coast on the Yucatan Peninsula, Mexico. The hurricanes were inferred from prominent fining-upward coarse-grained beds intercalated within fine-grained carbonate mud.

This work explores the use of sinkhole lakes in alluvial valleys as recorders of floods. The working hypothesis is that large flood events may deposit distinctive coarse-grained sediments in these lacustrine basins that normally have fine-grained background sedimentation. This geomorphic setting has similarities with oxbow lakes, which have been already used as proxies of past floods. For example, Oliva et al. (2016) reconstructed a 1300-yr-long record of paleofloods using sediment cores from two oxbow lakes along the broad floodplain of the Désert River in temperate-subpolar southwestern Québec, Canada. Here, flood deposits are detected through magnetic susceptibility peaks associated with fine-grained layers, intercalated within fine sediment rich in organic matter and lower values in magnetic susceptibility (Oliva et al., 2016). Sheffer et al. (2003) investigated paleofloods recorded in the deposits accumulated in a perched abandoned meander of the Ardèche River, southern France. The paleoflood record associated with a buried collapse sinkhole located in the floodplain of the Ebro River, northeastern Spain, which used to host a permanent pond, is investigated. Sinkholes in this area are related to the karstification of the evaporitic bedrock and are generally affected by high subsidence rates because of rapid dissolution of high-solubility beds (halite and glauberite).

GEOLOGIC SETTING

The investigated sinkhole is located in the middle reach of the Ebro River valley, northeastern Spain. The sinkhole pond, nowadays buried by anthropogenic deposits, is situated in the floodplain, 7 km to the west of Zaragoza city and 1 km to the southwest of Monzalbarba village (Figs. 1 and 2). From the geologic perspective, the site lies in the central sector of the Ebro Cenozoic basin, which is the southern foreland basin of the Pyrenean Alpine orogen. The valley has been carved in horizontally lying evaporites of the late Oligocene-Miocene Zaragoza Formation, deposited in an extensive high-salinity playa-lake system (Quirantes, 1978; Ortí and Salvany, 1997). This formation, more than 850 m in thickness, is composed of anhydrite ($CaSO_4$), halite (NaCl), glauberite ($Na_2[CaSO_4]_2$), and clay and marl in the subsurface. Secondary gypsum ($CaSO_4{\cdot}2H_2O$) is the only evaporitic rock exposed at the surface (Torrescusa and Klimowitz, 1990; Salvany et al., 2007; Salvany, 2009). On the basis of nine boreholes drilled along a 50-km-long stretch of the Ebro valley, this upper part of the evaporitic sequence has been subdivided into four lithostratigraphic units, in ascending order (Salvany et al., 2007; Salvany, 2009): (1) a marl and anhydrite basal unit, (2) a halite unit (up to 150 m), (3) a glauberite-halite unit (~50 m), and (4) an anhydrite unit. In two nearby boreholes (Utebo and Santa Inés 2), the contact between the anhydrite unit and the underlying glauberite-halite unit occurs at 130–150 meters above sea level (m asl) (Salvany et al., 2007). The elevation of the studied sinkhole (205 m asl) suggests that this subsidence feature is likely related to interstratal karstification of high-solubility salts. The equilibrium solubilities of gypsum, glauberite, and halite in distilled water at normal conditions are 2.4 g/L, 118 g/L, and 360 g/L, respectively (Langer and Offerman, 1982; Ford and Williams, 2007; Gutiérrez and Cooper, 2013).

GEOMORPHOLOGICAL SETTING

The northwest-to-southeast-trending Ebro valley displays a markedly asymmetric geometry, with a prominent and linear gypsum escarpment on the northeastern margin and a stepped sequence of terraces on the opposite side (Figs. 1 and 2). The terrace deposits are locally thickened, filling kilometer-sized basins generated by dissolution-induced synsedimentary subsidence, in which the alluvium may reach more than 50 m in thickness. The terrace deposits are dominated by channel gravel facies that record broad braided channels, whereas fine-grained floodplain and palustrine-lacustrine facies are abundant in the thickened alluvium and in paleosinkholes. The alluvial cover typically shows numerous gravitational deformations and paleosinkholes, mainly related to sagging and/or collapse subsidence mechanisms. The subsidence structures commonly also affect the underlying gypsiferous bedrock, indicating that they are largely related to interstratal karstification of salts (e.g., Gutiérrez et al., 2008, 2015; Guerrero et al., 2013).

The Ebro River flows along a low-gradient and broad floodplain approximately 5 km wide. The channel has a

https://doi.org/10.1017/qua.2017.23 Published online by Cambridge University Press

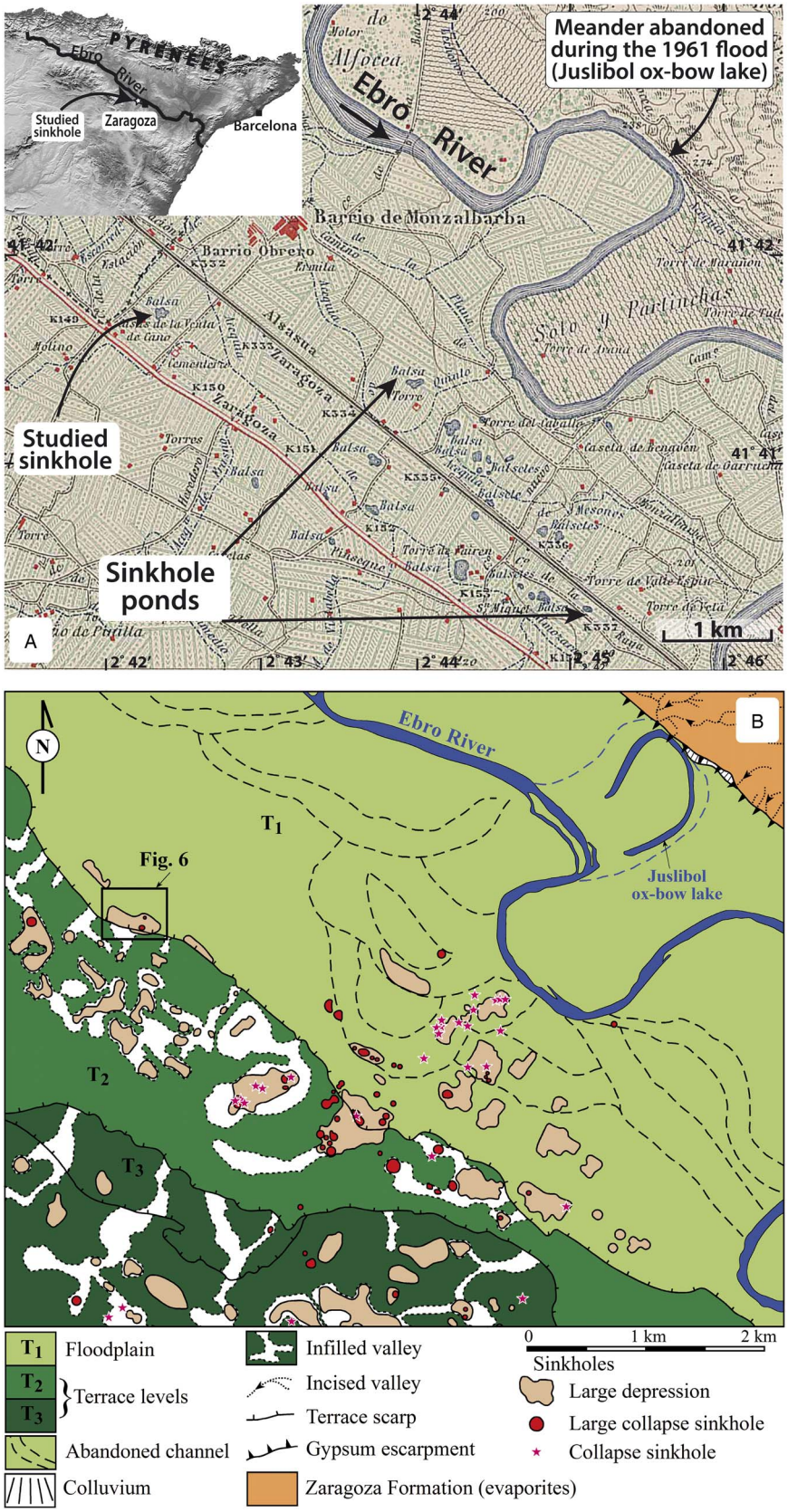

Figure 1. (color online) Geographic setting of the investigated sinkhole. (A) Excerpt of the 1:50,000-scale topographic sheet of Alagón (354) produced by the Dirección General del Instituto Geográfico Catastral in 1930 (first edition). The map shows the analyzed water-filled sinkhole before its anthropogenic infill, as well as numerous sinkhole ponds (locally known as *balsas* and *ojos*) mostly obliterated by anthropogenic deposits and human structures. Inset shows the general geographic location. (B) Geomorphological map of a section of the Ebro River valley including the analyzed sinkhole (modified from Galve et al., 2009).

https://doi.org/10.1017/qua.2017.23 Published online by Cambridge University Press

Figure 2. (color online) Orthoimage from 2002 and topographic profile showing the location of the studied sinkhole, the area covered by the 2003 flood, and the estimated limit of the 500 yr flood, according to the Ebro River Basin Water Authority.

https://doi.org/10.1017/qua.2017.23 Published online by Cambridge University Press

Figure 3. (color online) Examples of sinkhole ponds that intersect the water table in the floodplain of the Ebro valley. These are the Ojos de Matamala, located downstream of Zaragoza city. The circular sinkhole is 30 m across and is centered at 41°36.693' N 0°44.528' W. These actively subsiding depressions with lacustrine deposition may act as traps for detrital sediments during flood events.

sinuous geometry (sinuosity index of 1.6; Ollero, 2010) with gravelly point bars and midchannel bars. The floodplain, mainly occupied by crop fields, is underlain by fine-grained facies and shows multiple crosscutting abandoned channels, some oxbow lakes (locally known as *galachos*) (Fig. 1), and sinkhole ponds (Fig. 3). The Ebro River in its middle reach has experienced frequent changes mainly by migration and also by avulsion and cutoff processes (Regato, 1988; Ollero, 1995, 2010; Gutiérrez et al., 2007; Benito-Calvo et al., 2016). Magdaleno and Fernández-Yuste (2011), in a study on the evolution of the middle reach of Ebro River between 1927 and 2003, document a significant reduction in the mobility of the channel and its average bankfull width. Benito-Calvo et al. (2016) document a displacement of 540 m in the river channel at Alcalá village between 1927 and 1957, resulting in the abandonment of a river passage. These are largely episodic adjustments associated with flood events. For instance, the Juslibol oxbow lake, located 4 km northeast of the studied site, was created by the 1961 Great Ebro River Flood, which caused the cutoff of a meander (Ollero, 2010) (Fig. 1). At the present time, the potential for the river to change its path has been significantly restricted by the construction of channel-bank protection structures (e.g., riprap and concrete walls), dikes, and flood lamination using the headwater reservoirs (e.g., López-Moreno et al., 2002; Cabezas et al., 2009; Ollero, 2010). The integrity of the dikes is locally compromised by active sinkholes (Benito-Calvo et al., 2016).

The floodplain is affected by numerous active sinkholes (approximately 8% of the area underlain by evaporites) that can be grouped into three types (Galve et al., 2009): (1) sagging sinkholes hundreds of meters long with diffuse edges, (2) large collapse sinkholes tens of meters across, and (3) small cover collapse sinkholes (Fig. 1). The large collapse sinkholes commonly intercept the water table and consequently host permanent lakes that may reach more than 6 m in depth (Gutiérrez et al., 2007, 2011) (Fig. 3). These active sinkholes have been largely filled by anthropogenic deposits including a wide variety of materials (Fig. 1), and many of them have been used for the construction of human structures (e.g., buildings, roads, and conventional and high-speed railways) (Galve et al., 2009, 2015). Consequently, the area is affected by severe subsidence damage, mainly related to the activity of preexisting sinkholes improperly used for development. Galve et al. (2009), in a large area upstream of Zaragoza city (40.8 km^2), including the investigated sinkhole, estimated that approximately 70% of the sinkholes identifiable in aerial photographs from 1957 have been obliterated by human activity. The studied sinkhole, associated with the southern edge of the floodplain, is a large diffuse-edged depression with a nested collapse sinkhole that used to host a permanent pond (Figs. 4 and 5). The buried pond is located at the foot of the lowermost terrace (+8–10 m) and 2.4 km apart from the present-day river channel.

THE EBRO RIVER FLOODS

The Ebro River is the largest Mediterranean fluvial system of the Iberian Peninsula, with a watershed area of 85,362 km^2 and a channel length of 930 km. In its middle reach, around Zaragoza city, it is essentially an allochthonous drainage that flows across a semiarid area (300–400 mm/yr), conveying the runoff mostly contributed by the Pyrenean headwaters (Fig. 1), where the mean annual precipitation reaches more than 2000 mm. At Zaragoza gauging station, with a contributing area of 40,434 km^2, the mean annual discharge is 216.5 m^3/s (5.35 $L/s/km^2$). Here, the river has a pluvial-nival regime, with the highest monthly flow recorded in February and prolonged low flows in summer (Ollero, 2010).

Floods commonly occur in winter and in early spring and are typically related to long-lasting cyclonic rains in the Pyrenees that may induce rapid snow melting. The historical floods of the Ebro River in Zaragoza area compiled by the Comisión Nacional de Protección Civil (CNPC) are shown in Table 1 (CNPC, 1985). The oldest event dates back to AD 827. Most of these floods caused damage to bridges, crop fields, and villages located in the floodplain, and there is no information on the peak discharge. The largest flood of the nineteenth century occurred in January 1871, which caused several fatalities (CNPC, 1985; Espejo et al., 2008; Mejón, 2011). A smaller and spatially restricted flood in 1880 overturned a boat in Logroño (160 km upstream of Zaragoza) killing 90 soldiers. The biggest flood in the twentieth century was the Great Ebro River Flood of January 1961, with a peak flow rate of 4130 m^3/s at Zaragoza and a return period of around 80 yr according to the Ebro Basin Water Authority. This event, with higher magnitude than the 1871 event, was produced by a long rainfall episode accompanied by substantial snow melting in the Pyrenees. This is the largest and most damaging flood event within the instrumental record starting in 1943. The floodwaters caused severe economic

https://doi.org/10.1017/qua.2017.23 Published online by Cambridge University Press

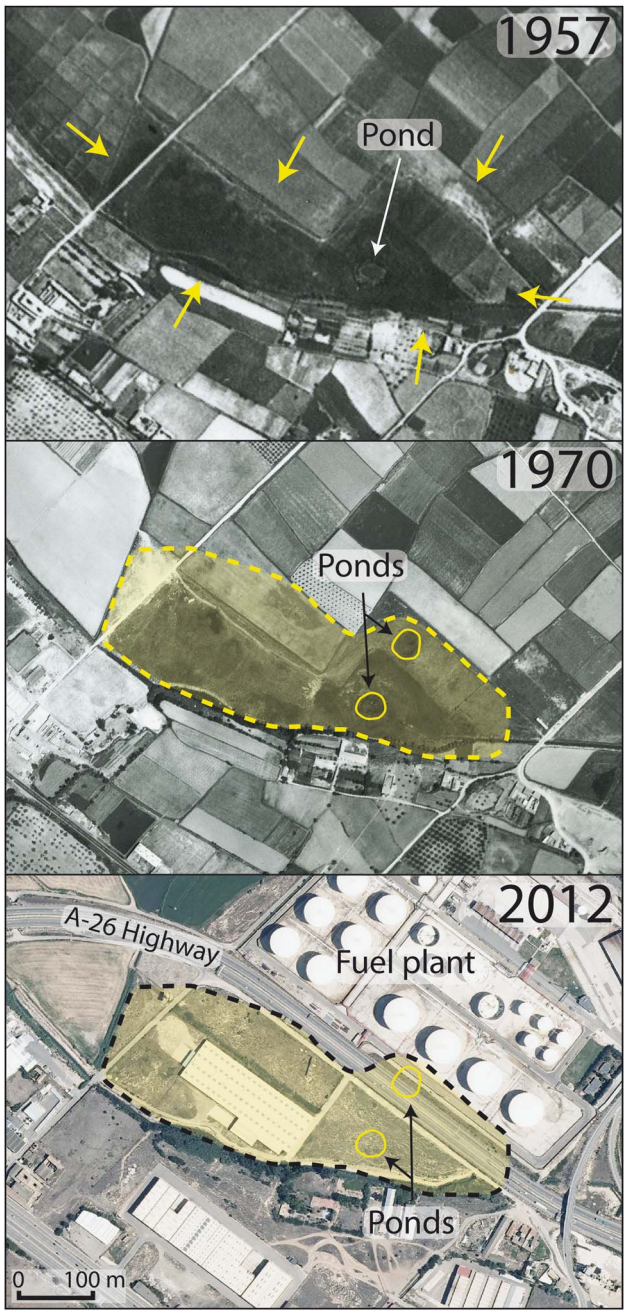

Figure 4. (color online) Aerial photographs of the investigated sinkhole located in the Ebro River floodplain. This complex sinkhole comprises a large diffuse-edged depression and a nested collapse sinkhole approximately 40 m across with a permanent pond. The image from 1970 with higher resolution allows the identification of an additional pond. The sinkhole was obliterated by artificial filling between 1970 and 1984 and used for the construction of human structures.

damage and had a major morphosedimentary impact, including significant changes in the route of the river channel and the formation of the Juslibol oxbow lake through a meander cutoff (CNPC, 1985; Ollero, 1995; Mejón, 2011) (Fig. 1). The February 1952 flood and the well-documented February 2003 flood were the second and fourth largest

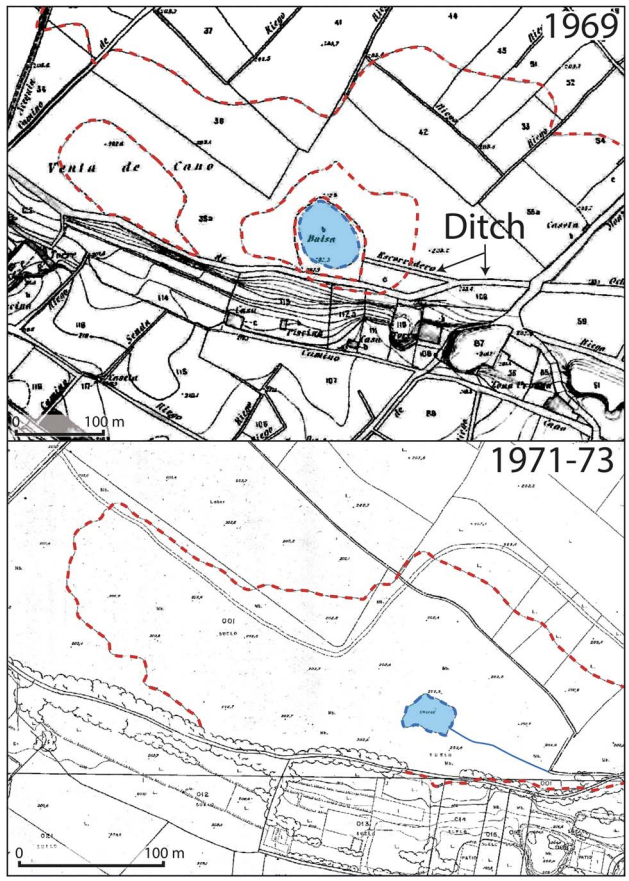

Figure 5. (color online) Detailed topographic maps of the Municipality of Zaragoza produced in 1969 (1:2000 scale, 1 m contour interval) and 1971–1973 (1:1000 scale, 2 m contour interval). Both maps depict the sinkhole pond (*balsa*) and a drainage ditch that used to flow into the pond. Dashed contour lines roughly illustrate the topography of the large subsidence depressions.

events that have occurred so far in the twentieth and twenty-first centuries, with peak discharges of 3260 m^3/s and 2988 m^3/s, respectively (Table 1). The floodwaters in the 2003 event covered 83% of the floodplain (Losada et al., 2004), but not the analyzed sinkhole. The peak discharge of floods that overflow the dikes exhibits a significant downstream decrease between Castejón and Zaragoza gauging stations, approximately 85 km apart, and a twofold increase in the propagation time of the hydrograph crest because of the laminating and retarding effect of the floodplain (Espejo et al., 2008). Moreover, some floodplain areas located beyond the dikes are frequently flooded by quasi-static waters related to water table rise. The magnitude and frequency relationships of floods have changed substantially in the second half of the twentieth century, involving a significant hazard reduction, mainly because of the construction of reservoirs (Batalla et al., 2004; Cabezas et al., 2009). The storage capacity of reservoirs upstream from Zaragoza is approximately 2700 hm^3, mainly related to the Reinosa (540 hm^3, 1945), Yesa (447 hm^3, 1960), and Itoiz reservoirs (586 hm^3, 2002).

https://doi.org/10.1017/qua.2017.23 Published online by Cambridge University Press

Table 1. Larger historical and instrumentally recorded floods of the Ebro River in the analyzed area. Peak discharge values before 1943 correspond to rough indirect estimates. The two largest floods of the nineteenth and twentieth centuries are indicated in bold.

Year (month)	Peak discharge (m^3/s)	Geomorphic effects	Damage	References
827, 1143, 1251, 1261, 1269, 1328, 1372			Bridge destruction	Comisión Nacional de Protección Civil (CNPC) (1985)
1380		Meander cutoff in Zaragoza		CNPC (1985), Mejón (2011)
1397, 1405			Bridge destruction	CNPC (1985)
1408		Change in river path at Zaragoza	Destruction of walls	CNPC (1985), Mejón (2011)
1415, 1420, 1434, 1435, 1445			Bridge destruction	CNPC (1985)
1461		Shift in river path		CNPC (1985)
1480				CNPC (1985)
1641		Shift in river path		CNPC (1985)
1642, 1643 (Feb), 1707, 1800, 1801, 1829, 1831			Damage on bridge	CNPC (1985), Mejón (2011)
1871 (Jan)			Several fatalities; some villages lost communication; partial flooding of Zaragoza	CNPC (1985), Mejón (2011)
1874 (Sep), 1878 (Mar)				CNPC (1985)
1880 (Aug)			Ninety fatalities (overturned boat with soldiers)	CNPC (1985)
1889 (Feb)	~3880			CNPC (1985)
1891 (Jan)	~3250		Extensive damage to crops	CNPC (1985)
1892 (Feb)	~3790		Extensive damage to crops	CNPC (1985)
1895 (Jan)	~3118		Extensive damage to crops	CNPC (1985)
1906 (Dec)	~3030		Extensive damage to crops	CNPC (1985)
1916 (Dec)			Extensive damage to crops	CNPC (1985)
1930 (Mar)	~3500	Channel shift of 600 m at Alcala	Major damage along the middle reach; partial flooding of Zaragoza; water stage slightly lower than in 1871	CNPC (1985), Ollero (2010), Mejón (2011), Benito-Calvo et al. (2016)
1936 (Feb)			Flooding in outer suburbs	CNPC (1985)
1937 (Oct)	~3050		Fatalities in the lower valley reach	CNPC (1985)
1941 (Jan)	~3150		Bridge destruction	CNPC (1985)
1952 (Feb)	3260		Extensive damage to crops	CNPC (1985)
1961 (Jan)	4130	Creation of the Juslibol oxbow lake by meander cutoff	Villages flooded and isolated; cuts in communication infrastructure; partial flooding of Zaragoza; >615 million pesetas worth of damage	CNPC (1985), Ollero (2010), Mejón (2011)
1966 (Nov)	3154		Extensive damage to crops and dikes	CNPC (1985), Mejón (2011)
1978	2631			Mejón (2011)
1980 (Dec)	2908		Extensive damage to crops and flooding of riverine villages	CNPC (1985)
1981 (Jan)	2940			Espejo et al. (2008)
2003 (Feb)	2988	Eighty-three percent of the floodplain inundated		Losada et al. (2004), Ollero (2010)
2007 (Apr)	2282	Fifty-seven percent of the floodplain inundated		Espejo et al. (2008), Ollero (2010)
2015 (Mar)	2448		Extensive damage to crops (~140 million euros)	Confederación Hidrográfica del Ebro (2015)

METHODOLOGY

Before exploring the potential paleoflood record associated with the large depression and the nested pond, we applied several methods in order to characterize this complex sinkhole. Priority was given to the following issues: (1) definition of the edges of the large depression and the nested sinkhole pond; (2) identification of potential paleoflood deposits along the edge of the terrace, which is affected by the large sinkhole, and the buried sinkhole pond; (3) internal geometry of the compound sinkhole; and (4) long-term evolution of the subsidence structure and current activity. Initially, we analyzed old aerial photographs and topographic maps that show the large depression and the nested sinkhole pond before its filling (Figs. 4 and 5). The aerial photographs were orthorectified and georeferenced with a geographic information system in order to map the edges of the infilled depressions. Particularly useful were images taken in 1927 (Fotoplano of the Ebro Basin Water Authority), 1946 (American flight A), 1957 (American flight B), and 1970 (Fig. 4). The location of the sinkhole pond was also constrained using old detailed topographic maps of the Municipality of Zaragoza produced in 1969 (1:2000 scale, 1 m contour interval) and 1971–1973 (1:1000 scale, 2 m contour interval) (Fig. 5).

A detailed field survey was conducted in the area, paying special attention to the identification of evidence of recent deformation, both on the ground surface and in the human-built structures (Fig. 6). These features were used to refine the limits of the area affected by subsidence and assess its activity. Subsequently, we excavated five trenches, four of them on the terrace next to its riser (T1–T4) and another one in the floodplain within a crop field in the western sector of the large depression (T5). Trenches T1 to T4 were aimed at defining the southern edge of the large sinkhole and exploring the probable existence of paleoflood deposits on a minor bench associated

https://doi.org/10.1017/qua.2017.23 Published online by Cambridge University Press

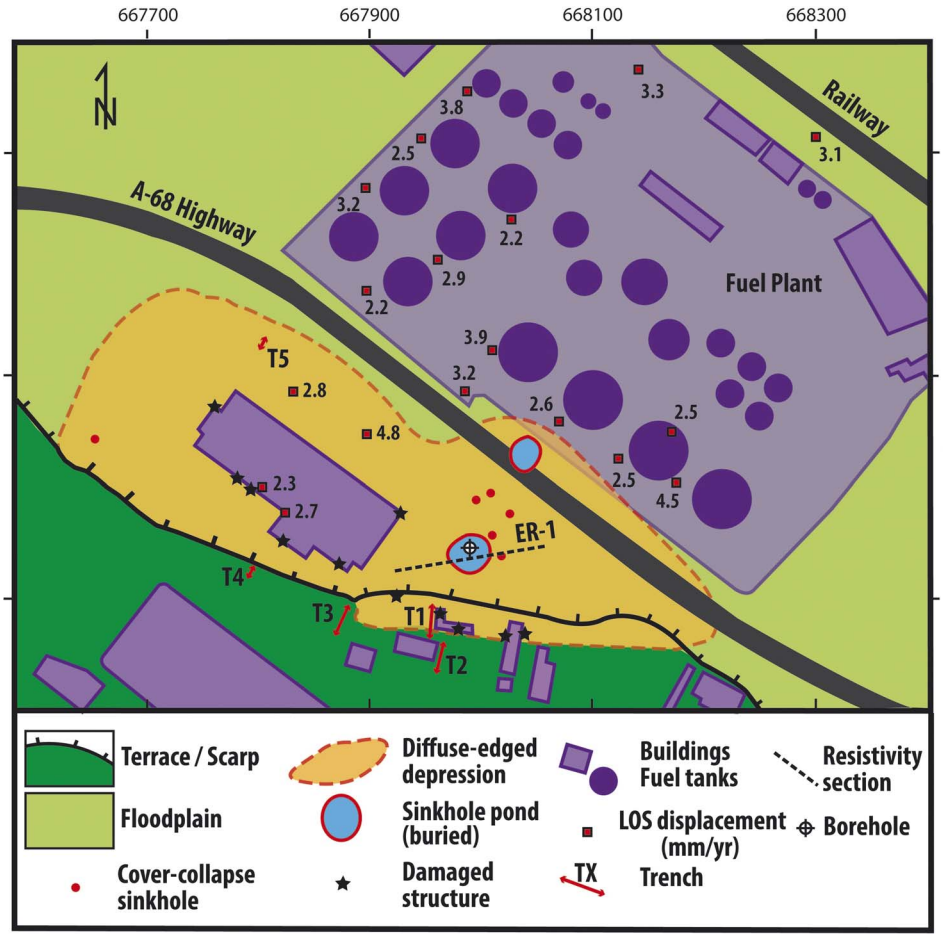

Figure 6. (color online) Map of the investigated complex sinkhole showing the distribution of geomorphic units, subsidence features, location of damage identified on human structures, DInSAR (differential interferometry synthetic aperture radar) deformation data, trenches, the electrical resistivity section acquired across the buried sinkhole pond, and borehole drilling in its central sector. LOS, line of sight.

with the terrace scarp. Trenches were excavated with a rubber-tired backhoe. The vertical walls were cleaned, and one of them was logged on graph paper using a reference grid with horizontal and vertical strings spaced 1 m apart. Samples were collected for accelerator mass spectrometry (AMS) dating giving priority to the most adequate stratigraphic units for determining the age of flood deposits. The deformation and sedimentation history recorded in trench T1 was reconstructed by performing a retrodeformation analysis (e.g., McCalpin, 2009a; Carbonel et al., 2014, 2015).

Ground deformation data derived from differential interferometry synthetic aperture radar (DInSAR) displacement rate maps have been integrated in the sinkhole characterization (Fig. 6). Subsidence rates were derived from 29 ENVISAT ASAR images acquired from May 2, 2003, to September 17, 2010. The data were processed using the Stable Point Network persistent scatters (PS) approach (Arnaud et al., 2003; Crosetto et al., 2008), through which coherent points (20 m pixels) were identified considering a coherence threshold of >0.46 and a deviation amplitude of <0.50. In this study, we have considered subsidence rates higher than 2 mm/yr, based on the assessed error margin (Galve et al., 2015).

An electrical resistivity section was acquired across the buried sinkhole pond (i.e., Griffiths and Barker, 1993; Loke et al., 2013). The bulk electrical resistivity in alluvial environments is largely governed by the grain size of the different units. Therefore, electrical resistivity tomography (ERT) was a priori an adequate method to image the clayey lacustrine-palustrine facies of the large subsidence depression and the nested sinkhole pond, overlain by coarse and porous anthropogenic deposits and underlain by fluvial gravels. Moreover, this geophysical method is particularly useful for obtaining information on the internal geometry of sinkholes below the investigation depths of other techniques (e.g., ground penetrating radar, trenching; Carbonel et al., 2014; Zarroca et al., 2016). The ERT profile was acquired with the multielectrode Lund Imaging System (ABEM) and interelectrode spacing of 2 m. The system is composed of a Terrameter SAS 4000 resistivity meter, an electrode selector ES10-64, a four-signal cable and reels, and 64 steel electrodes. We selected a dipole-dipole electrode array (Dahlin and Zhou, 2004), and the measured apparent resistivity data were processed using the two-dimensional finite-difference inversion commercial software RES2DINV of Loke and Barker (1996) to produce the resistivity image.

https://doi.org/10.1017/qua.2017.23 Published online by Cambridge University Press

Table 2. Code of samples dated by accelerator mass spectrometry, site, laboratory number (Poznan Radiocarbon Laboratory), material, conventional radiocarbon ages, and calibrated age ranges with an error margin of 2-sigma (using CALIB 7.1 and the data set IntCal 13; Reimer et al., 2013). Figures in parentheses indicate the relative area under the probability curve.

Sample code/site	Laboratory number	Material	Conventional ^{14}C age (yr BP)	Calibrated date (2σ) (BC/AD)	Calibrated date (2σ) (yr BP)
VCT6-2/ trench 1	Poz-36766	Shells	6050 ± 40	5054–4838 BC	7004–6788
VCT8-96/ trench 5	Poz-36767	Shells	1725 ± 40	AD 245–388	1705–1562
SVC34ii/ borehole	Poz-37265	Charcoal	2560 ± 40	809–731 BC (0.538)	2759–2681
				691–660 BC (0.109)	2641–2610
				650–544 BC (0.353)	2600–2494
SVC16i/ borehole	Poz-36959	Charcoal	1530 ± 60	AD 413–639	1537–1311
SVC10iii/ borehole	Poz-37143	Charcoal	Modern	>AD 1950	-

A 20-m-long borehole with full-core recovery was drilled in the central sector of the sinkhole pond filled between 1970 and 1984. Some deposits of the core underwent considerable compaction during the drilling operations, especially the clayey lacustrine facies. To construct the stratigraphic log, the original thickness of the different units was estimated by applying a backstripping factor for each section of the core given by the ratio between the length of the borehole section and the length of the retrieved compacted core. This factor was generally lower than 1.5. The core was longitudinally halved in the laboratory, and the stratigraphic units were differentiated by visual examination, mainly on the basis of their textural characteristics, color, and internal structure. Three charcoal samples were collected for AMS dating. The obtained conventional radiocarbon ages were calibrated using CALIB 7.1 and the data set IntCal 13 (Table 2). The number of dated samples was constrained by budget limitations, rather than by the availability of datable material.

SINKHOLE CHARACTERIZATION

Aerial photographs, topographic maps, and field surveying

The aerial photographs from 1927, 1957, and 1970 show a shallow depression oriented west/northwest–east/southeast with palustrine vegetation approximately 600 m long and 240 m wide (Fig. 4). This large sinkhole is apparently confined to the floodplain with its southern edge located at the foot of the lower terrace (Simón Gómez et al., 1998; Galve et al., 2009). The northern edge of the topographic depression is defined by rectilinear scarps associated with crop fields, suggesting that its extent has been reduced by anthropogenic filling in order to increase the cultivable land. The three aerial photographs clearly show a nested sinkhole pond approximately 40 m in diameter on the eastern half. The images from 1970, with higher resolution, allow the recognition of another pond, apparently shallower, nowadays located beneath the A-68 highway (Fig. 6). Aerial photographs from 1984 show the depressions completely buried and a large fuel plant built along its northern margin (i.e., the sinkhole was obliterated sometime between 1970 and 1984). The detailed topographic maps produced in 1969 and 1971–1973 roughly depict the large depression with dashed contour lines, and the nested sinkhole is represented as a pond (*balsa*) 80 and 40 m across, respectively (Fig. 5). Elevation data in the 1971–1973 map indicate that the large depression was at least 1.5 m deep. Both maps show an old drainage ditch (*escorredero*) that used to flow into the pond.

The walls of the factory located in the western sector of the depression show numerous curved subhorizontal cracks with apertures of up to 10 mm indicative of basal support loss and differential settlement (Fig. 6). Severe subsidence damage was detected in a concrete ditch and buildings located on the terrace, next to its riser. The presence of these recent deformation features on the northern sector of the terrace led us to consider that the sinkhole is not confined to the floodplain, and that its southern edge might be located on the terrace. This interpretation would help to explain a secondary bench associated with the terrace scarp, which might include paleoflood deposits.

Trenching and slack-water paleoflood deposits

In order to test the hypothesis indicated previously on the southern boundary of the sinkhole, we excavated four trenches (T1–T4) along the northern edge of the terrace and oriented roughly perpendicular to the scarp (Fig. 6). Trenches T2, T3, and T4, up 3.5 m deep and approximately 41, 22, and 12 m long, respectively, exposed crudely bedded terrace gravels with no evidence of deformation.

Trench T1 was excavated with an N12E orientation next to a building affected by conspicuous cracks parallel to the adjacent terrace scarp (Fig. 7). The excavation was 25 m long and reached a depth of 2.4 m, limited by flooding of the trench bottom by groundwater coming from the gravels exposed in the southern sector (perched aquifer). The terrace gravels occur in two blocks separated by a deformation zone approximately 1.5 m wide. This deformation band comprises, from north to south: (1) an oversteepened down-to-the-north normal fault with an associated shear zone overlain by a colluvial wedge and (2) a downward-tapering fissure fill opened between the terrace gravels of the footwall and the colluvial wedge underlain by the shear zone of the downthrown block (i.e., the

https://doi.org/10.1017/qua.2017.23 Published online by Cambridge University Press

fissure clearly postdates the colluvial wedge). The shear zone, 0.6 m wide, is made up of terrace gravels with reoriented fabrics, and its northern edge is defined by a fault plane dipping antithetically 65°S. This pseudoreverse fault is in fact a normal fault rotated toward the sinkhole during the development of the fissure. The colluvial wedge is 0.4 m thick and 2 m long, and its base dips around 8° to the north. It is made up of poorly sorted and matrix-rich rounded gravels shed from the fault scarp underlain by terrace gravels. The orientation of the planar clasts is roughly concordant with the top boundary of the wedge. The fissure fill, 1 m wide in the upper part, consists of a well-cemented deposit including two units separated by a downward-pointing V-shaped contact. The lower unit is gravel with silt matrix and chaotic fabrics, and the upper unit massive marly silts. The top of the terrace gravels on both sides of the deformation band (shear zone and fissure) shows a vertical separation of 0.7 m. This is consistent with the rule of thumb whereby the thickness of colluvial wedges tends to be half of the height of the fault scarps from which they are derived (McCalpin, 2009b). Most probably, the top of the terrace gravels in the footwall has experienced some erosion. The vertical separation of the upper contact of the terrace gravels rises to 1.75 m considering the whole length of its exposure in the trench.

In the downthrown block, there is a fine-grained deposit that overlies the terrace gravels and the colluvial wedge. This unit pinches out just at the northern edge of the fissure. This deposit consists of light-brown massive fines, from coarse sand to silt, with normal grading and abundant gastropods. In the northern sector of the trench, it includes thin lenticular beds of pebbly-granule gravel (Fig. 7). Shells collected 35 cm below the top of this unit have yielded a calibrated age of 7004–6788 cal yr BP (2-sigma error). This unit is interpreted as a mid-Holocene slack-water paleoflood deposit (Baker, 1987) of the Ebro River, most probably formed when the river channel was located at a higher elevation; the deposit lies at approximately 6 m above the current floodplain. The paleoflood deposit is tilted toward the sinkhole. The top of the unit dips 3°–4°, and the dip of the intercalated gravel bed reaches 5°–6° in the northern sector of the trench. Moreover, the deposit is affected by a small monoclinal fold around the vertical reference lines 5–7, probably related to a secondary buried normal fault (drape fold). The top of the unit shows an elevation difference of 1.2 m along the trench. The deformed units of the footwall, the deformation zone, and the downthrown block are overlain by two apparently nondeformed anthropogenic deposits that thicken toward the north, indicating that the sinkhole at this site used to have geomorphic expression in historical times.

The stratigraphic and structural relationships observed in the trench allow us to infer the following deformational and depositional history, as illustrated in a simplified retrodeformation sequence (Fig. 8). A first collapse event, older than 7 ka and controlled by a subvertical normal fault, caused the downdropping of a portion of the terrace and the generation of a lower bench. The displacement along the fault of approximately 1 m produced a shear zone, and erosion on the oversteepened fault scarp resulted in the development of the colluvial wedge. Subsequently, a flood of the Ebro River, dated at 7004–6788 cal yr BP, deposited a package of fine-grained sediments (slack-water deposits) on the bench onlapping the colluvial wedge. Later, the downthrown block experienced a rotation toward the sinkhole center, with the consequent opening of a fissure. The two units in the fissure fill with a synformal structure may be related to downward raveling and compaction and/or two episodes of fissure opening. The total vertical displacement accommodated in this second deformation event in the trench zone was approximately 1.2 m. Subsequently, the geomorphic expression of the sinkhole margin was masked by the accumulation of artificial deposits. Although these massive anthropogenic deposits do not show evidence of deformation, the conspicuous damage observed in the adjacent building reveals that this sector of the sinkhole is still active.

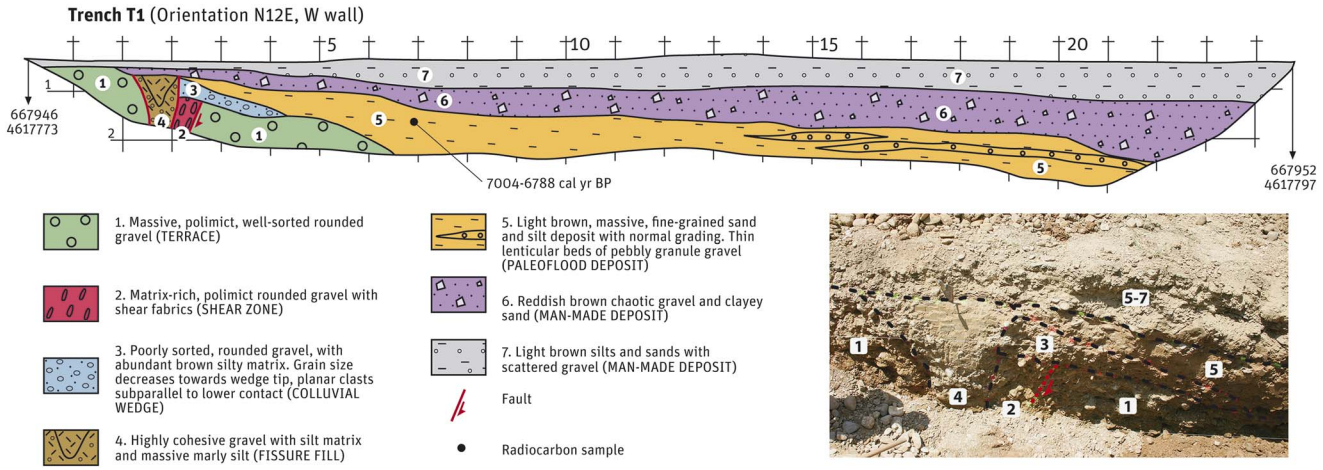

Figure 7. (color online) Trench T1 excavated next to the terrace scarp. It revealed the southern edge of the large depression on the terrace through a deformation band including a down-to-the-north oversteepened fault and a younger fissure fill (shown in inset image). The downthrown block has fine-grained slack-water deposits related to a mid-Holocene Ebro River flood.

https://doi.org/10.1017/qua.2017.23 Published online by Cambridge University Press

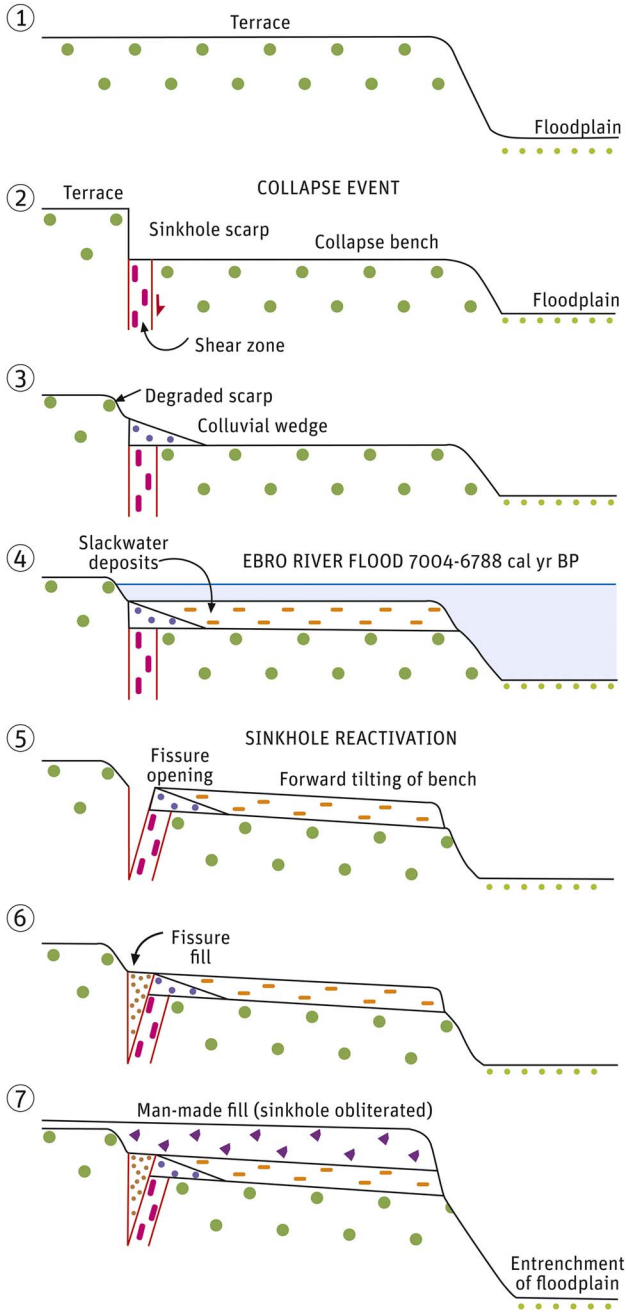

Figure 8. (color online) Simplified retrodeformation sequence derived from the stratigraphic and structural relationships observed in trench T1. In stage 2, it is assumed that subsidence in the floodplain is counterbalanced by aggradation.

The southern edge of the large sinkhole was mapped integrating the distribution of subsidence damage on human structures and the trenching investigation, including a portion of the northern sector of the terrace (Fig. 6). The proposed extent excludes trenches T2, T3, and T4, adjusts the edge to the deformation zone exposed in trench T1, and embraces the recorded subsidence damage.

Trench 5 was excavated in the northwest sector of the large depression, within a crop field located in the floodplain (Fig. 6). The excavation, 6 m long and 2 m deep, exposed, from top to bottom: (1) a gravelly anthropogenic deposit 65 cm thick; (2) 115 cm of dark-brown, massive, and bioturbated mud with scattered granules and abundant gastropods and vegetation remains; and (3) the upper part of a bed of lose rounded gravel. Shells collected from the palustrine facies 20 cm above its base yielded a calendar age of 1705–1562 cal yr BP. The data provided by this trench reveal that this sector, although leveled by anthropogenic fill, forms part of the large depression, and that this part of the sinkhole was occupied by a palustrine environment in the Ebro River floodplain at least since the third century AD.

DInSAR deformation data

The available DInSAR ground deformation data are essentially restricted to human structures and paved areas because of lack of coherence in crop fields and wastelands, including the buried sinkhole pond. Deformation data points tend to be distributed in clusters with similar values, from which we have depicted the highest ones in Figure 6. Consistent with the geomorphological map, mean subsidence rates along the line of sight (LOS) on the western sector of the large depression, including the damaged factory, range from 2.3 to 4.8 mm/yr (Fig. 6). The DInSAR displacement rate map also captures stable pixels in buildings located outside the mapped boundary of the large sinkhole, like the large factory situated on the terrace. In apparent contradiction with our geomorphological map, the fuel plant shows numerous deformation points (2.2–4.5 mm/yr), mainly clustered on the southwestern side of the tanks. This disagreement may be related to artifacts caused by double-bounce reflection. Double bounce is a type of scattering behavior frequent in built-up areas and depends on the geometric relationship between the sensor flight line and the feature orientation (Henderson and Lewis, 1998). Considering the ascending right-looking pass of the images and the incidence angle of the ENVISAT ASAR satellite (20°–30°), clusters of double-bounce PS points may have formed because of the bouncing effect of the tank walls (~16 m high).

ERT

The 126-m-long electrical resistivity section was acquired across the buried sinkhole pond with an ENE-WSW orientation and approximately centered on its middle point (Figs. 6 and 9). The interpretation of the resistivity model has been aided by knowledge on the geomorphic setting and the 20-m-deep borehole drilled in the center of the sinkhole pond, which traversed, from top to bottom, three sedimentary packages: (1) a coarse anthropogenic fill, 3.9 m thick; (2) a sinkhole fill, 7.85 m thick, consisting of clayey facies with some gravel intercalations; and (3) fluvial gravels more than 8.25 m thick (the base of the alluvial cover was not reached). Consistent with the borehole data, the resistivity image shows three electrolayers. The upper layer with medium-high resistivity (50–500 Ωm) corresponds to the anthropogenic deposits. In the central sector of the buried sinkhole pond, between stations

https://doi.org/10.1017/qua.2017.23 Published online by Cambridge University Press

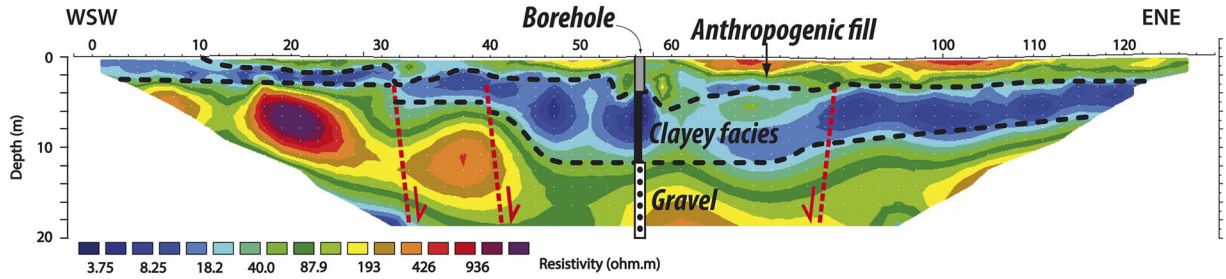

Figure 9. (color online) Electrical resistivity section acquired in June 2011 across the buried sinkhole pond with a dipole-dipole array and an interelectrodic spacing of 2 m.

52 and 62, it displays an abrupt thickening (~6 m) that might be related to a collapse structure nested within the sinkhole pond. The intermediate low-resistivity layer (<10 Ωm) is ascribed to clayey sediments deposited in the palustrine and lacustrine environments developed in the large depression and the inner sinkhole pond, respectively. The thickness of this unit increases from 1 to 4 m in the margins of the section, to approximately 8 m in the sinkhole pond, consistent with the borehole log. Its base, especially in the western half of the resistivity image, shows abrupt drops toward the sinkhole center attributable to collapse faults. The central sector where the intermediate layer reaches the greatest thickness is approximately 40 m wide, in agreement with the diameter of the sinkhole pond. The lower medium-high resistivity layer (>75 Ωm) corresponds to the coarse fluvial gravel logged in the borehole. The stepped geometry of the top of this unit, as well as the heterogeneous distribution of the resistivity, could be related to the aforementioned collapse faults. Overall, the resistivity image indicates that this is a large sagging sinkhole (large depression) with an inner collapse structure (sinkhole pond) controlled by a master ring fault approximately 40 m in diameter and other secondary outer and inner collapse faults.

SINKHOLE POND FILL AND PALEOFLOOD RECORD

Three main sedimentary packages comprising 35 stratigraphic units were differentiated in the 20-m-long borehole core obtained from the central sector of the buried sinkhole pond (Figs. 6 and 10). The uppermost package, corresponding to unit U1, is an anthropogenic deposit, 3.9 m thick, consisting of massive and chaotic matrix-rich gravel and rubble. The thickness of this artificial fill, dumped between 1970 and 1984, indicates that by that time the sinkhole pond was approximately 3–4 m deep. The lowest package, designated as unit U35, is composed of more than 8.25 m of relatively well-sorted, rounded, polimict pebble-cobble gravel with sand matrix, ascribed to channel facies. The borehole did not reach the base of the Quaternary cover. The 7.85-m-thick intermediate package includes units U2 to U34. This is a natural sinkhole fill, mainly composed of dark clays with intercalations of gravel and silt-sand beds. Four lithofacies types have been differentiated in the intermediate package as follows:

- I: Dark-brown/gray clay, commonly massive, but locally vaguely laminated. These soft clays generally contain plant remains, gastropods, and traces of bioturbation. The layers of this facies range from 2 to 59 cm thick and have an aggregate thickness of 5.5 m (67% of the natural sinkhole fill). This facies records low-energy lacustrine deposition in the freshwater sinkhole pond with relatively high production of organic matter.
- II: Thick beds of massive and rounded pebble gravel with a high proportion of light-brown sand-silt matrix. This gravel facies, intercalated within the clayey lake deposit, is represented by units U9 and U15, with thicknesses of 67 and 76 cm, and clasts up to 8 and 4 cm long, respectively. Facies II represents 17% of the natural sinkhole fill. These beds are ascribed to two major Ebro River floods, during which the floodwaters reached flow competence conditions high enough to transport gravels across the low-gradient floodplain. Sudden water depth increase at the sinkhole pond and the consequent energy dissipation prompted rapid sediment load deposition.
- III: Thin beds (2–8 cm thick) of rounded pebble gravel with clayey silt matrix (units U3 and U7).
- IV: Silt-sand beds 6–69 cm thick with rounded pebble-sized clasts up to 4 cm long.

Facies III and IV can be attributed to different processes. Our preferred interpretation is that they correspond to flood events with significantly lower competence than those recorded by the thick gravel beds. Units U14, U10, and U16, in contact with the thick gravel beds, may have been deposited during the two large floods, before and after peak flow conditions. Other plausible interpretations, considering the geomorphic context, include storm-derived water flows coming from the adjacent terrace scarp (Fig. 6) and accumulation of alluvium transported by subaqueous mass movements from the scarped margins of the collapse sinkhole.

Charcoal samples from units U34 (base of intermediate package) and U16 (overlain by gravel unit U15) yielded calibrated ages of 2759–2681 and 1537–1311 cal yr BP,

https://doi.org/10.1017/qua.2017.23 Published online by Cambridge University Press

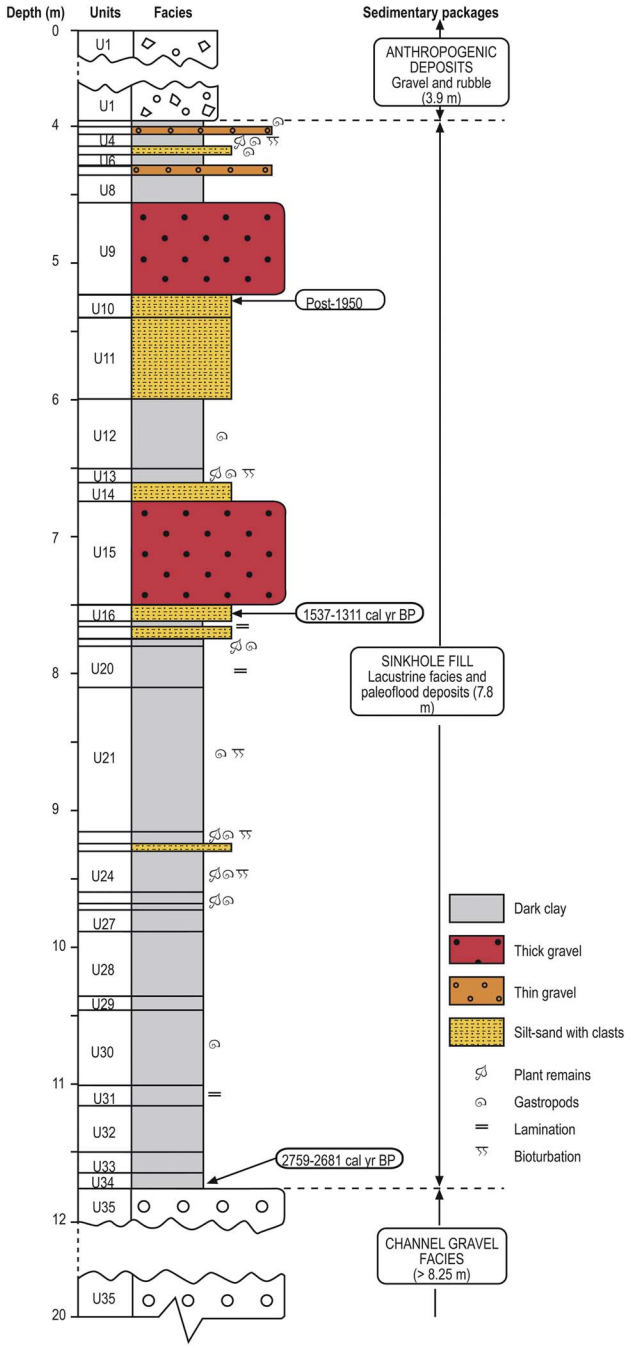

Figure 10. (color online) Stratigraphic log of the 20-m-deep borehole drilled in the central sector of the buried sinkhole pond.

respectively (Table 2). The sample from the top of unit U10 (overlain by gravel unit U9) provided a ^{14}C concentration of 131±039 pMC, indicating an age younger than 1950. The numerical age obtained from the top of unit U10 (>1950), situated just below the youngest thick gravel bed (U9), strongly suggests that the latter was deposited during the Great Ebro River Flood of January 1961. The age range obtained for unit U16 (1537–1311 cal yr BP, error margin at 2-sigma) should cover the calendar age of the flood recorded by the overlying thick gravel bed U15. This paleoflood, which occurred in Visigothic times, is older than the oldest flood documented from historical data, which dates back to AD 827 (CNPC, 1985).

The numerical ages also allow for inferring the following information on the evolution of the sinkhole: (1) The development of the collapse sinkhole and the creation of the sinkhole pond occurred at around 2759–2681 cal yr BP. (2) An average long-term subsidence rate of approximately 4.2–4.6 mm/yr can be computed considering the age of the sinkhole and the cumulative subsidence given by the aggregate thickness of the two upper packages (11.7 m). Although subsidence in the sinkhole is probably characterized by episodic kinematics, this value is consistent with the rates measured and estimated by various methods in active sinkholes of the salt-bearing evaporite karst of the Ebro valley (e.g., Galve et al., 2009, 2015; Desir et al., 2016). (3) Average aggradation rates between deposition of units U34–U16 and U16–U10 were approximately 3.4 and 1.6 mm/yr, respectively. The overall vertical accretion rate has decreased more than 50% in the last 1400 yr, despite that the two thick gravel beds (143 cm), which represent quasi-instantaneous deposition, were accumulated within this time span.

DISCUSSION

The subsidence depression used to explore the potential of sinkholes in alluvial systems as archives for flood events is located in the mantled evaporite karst of the Ebro River valley, upstream of Zaragoza city, northeastern Spain. The integration of the data gathered by geomorphological mapping, surveys of structural damage, trenching, ERT, DInSAR, and a borehole reveals the following features on the selected sinkhole:

1. The depression is a complex sinkhole comprising a large diffuse-edged basin approximately 600 m long and 240 m wide associated with the southern edge of the floodplain and the adjacent terrace, and a main nested collapse sinkhole that used to host a permanent lake approximately 40 m across (Fig. 6).
2. The spatial distribution of damage on human structures and a trench dug next to the terrace riser indicate that the southern edge of the large depression is located on the terrace, as revealed by a buried scarp, a colluvial wedge, and a fissure fill exposed in the trench. Episodic dissolution-induced subsidence on the terrace created a bench associated with the terrace riser, on which at least one Ebro River paleoflood, dated at 7004–6788 cal yr BP, accumulated fine-grained slack-water deposits (Figs. 7 and 8).
3. The sinkhole pond, located in the floodplain at the foot of the terrace scarp, was filled by anthropogenic deposits sometime between 1970 and 1984 (Fig. 4). By that time, water depth, controlled by the water table of the alluvial aquifer, was approximately 3–4 m. This pond, as suggested by the ERT section, was the

https://doi.org/10.1017/qua.2017.23 Published online by Cambridge University Press

geomorphic expression of a collapse structure, probably comprising a master ring fault approximately 40 m in diameter, and other outer and inner secondary concentric faults (Fig. 9).

4. Multiple lines of evidence indicate that both the large depression and the nested collapse sinkhole are currently active. DInSAR ground deformation data indicate LOS displacement rates on the order of 2–5 mm/yr in some sectors of the large depression (Fig. 6). Consistently, the numerical age of the oldest unit of the sinkhole-pond fill (2759–2494 cal yr BP), located at a depth of 11.7 m, indicates a long-term subsidence rate of 4.2–4.6 mm/yr (Fig. 9). These high subsidence rates strongly suggest that the sinkhole is related to interstratal dissolution of high-solubility salts (halite and or glauberite) (e.g., Castañeda et al., 2009; Galve et al., 2015; Desir et al., 2016).

Although unexpected, trench T1 dug next to the terrace scarp exposed a mid-Holocene slack-water paleoflood deposit accumulated in a peculiar geomorphic setting (i.e., an inset bench formed by collapse faulting at the margin of a large karst depression). The age of the slack-water deposits (7004–6788 cal yr BP) is older than the stratigraphic record of the sinkhole pond and falls within a period of increased fluvial activity in Spain at 7980–6860 cal yr BP (Thorndycraft and Benito, 2006), using a compilation of 74 Holocene radiocarbon dates. These sediments allow for obtaining information on the chronology of a prehistorical flood, but they cannot be used as paleostage indicators for paleodischarge estimation for two reasons: (1) the slack-water deposits have been affected by postsedimentary subsidence (>1.2 m), and (2) the sediments occur in a nonstable alluvial valley reach, whose bottom was probably at higher elevation around 7 ka ago.

The limited radiocarbon dates obtained from the sinkhole pond deposits provide a fairly weak age-depth structure. Nonetheless, the available numerical ages allow the inference of relevant features related to the subsidence and sedimentation patterns, including paleoflood deposits. Sedimentation in the sinkhole pond between 2759–2681 cal yr BP and 1970–1984 was dominated by lacustrine dark clayey facies, eventually interrupted by the accumulation of three types of coarser detrital facies: (1) two thick pebble gravel beds (>0.5 m thick), (2) thin layers of pebble gravel (<10 cm thick), and (3) silt-sand units with scattered pebble-sized clasts. The thick gravel beds, and probably the underlying and overlying sand-silt facies, record two major Ebro River floods with an interevent interval of 1300–1550 yr. During these events, fine gravel transported across the floodplain was rapidly accumulated in the sinkhole pond. Local flow energy dissipation at this sediment trap because of sharp increase in water depth caused rapid gravity-controlled deposition of massive gravelly facies with abundant sand-silt matrix. To our knowledge, this is the first paleoflood record from a sinkhole fill documented in the literature. The lower thick gravel bed records a paleoflood that probably occurred in Visigothic times between 1537 and 1311 cal yr BP, before the oldest flood documented with historical data, which dates back to AD 827 (Table 1; CNPC, 1985). The upper one is younger than 1950 as indicated by radiocarbon dating and older than the anthropogenic infill of the sinkhole pond bracketed at 1970–1984. Consequently, this unit is ascribed to the 1961 Great Ebro River Flood, with an estimated peak discharge of 4130 m^3/s. This is by far the biggest flood of the instrumental period starting in 1943, and probably larger than all the historical events (Table 1; Mejón, 2011). The Ebro River Basin Water Authority, based on the annual maximum discharge values recorded from 1943, estimates a return period of around 80 yr for the 1961 flood. Probably, that event is an outlier that biases the magnitude and frequency scaling relationships, leading to overestimated discharge values for high-recurrence periods (e.g., Webb et al., 2002). The thin gravel beds and the sand-silt units separated from the thick gravel beds by lacustrine facies may have been generated by lower-competence floods at the site. Nonetheless, they could also be related to other processes such as storm-derived water flows coming from the adjacent terrace scarp or subaqueous sediment-gravity flows originated from failures in the scarped margin of the collapse sinkhole. The palustrine facies dated in trench 5 are probably correlative to the fine-grained facies (units U14 and U13) that overlie the thick gravelly paleoflood deposit of the sinkhole pond. There is the possibility that the gravels underlying the palustrine facies of trench 5 could correspond to the first major paleoflood identified in the deposits of the sinkhole pond.

The investigated geomorphic settings have significant limitations as paleoflood recorders that affect their usefulness for flood-frequency analysis. Sinkhole sediments may considerably underrepresent the paleoflood history. The potential for a flood to be recorded in a sinkhole pond located in a broad floodplain and the sedimentologic signature of the deposits may depend on factors independent of the magnitude of the event, like the distance to the shifting channel, presence of riparian and palustrine vegetation (Fig. 3), flood duration, or the geometry and size of the sinkhole. Moreover, no flood magnitude estimates can be obtained from these stratigraphic records because they do not allow the inference of paleostage data. Paleocompetence methods based on the size of the largest particles may be applied to roughly estimate flow velocity (e.g., Maiziels, 1983; Williams, 1984), but this variable may also be affected by some of the local factors indicated previously.

Despite the aforementioned limitations, sinkhole ponds have some advantages: (1) In the case of active sinkholes, long-sustained subsidence higher than the aggradation rate facilitates the accumulation and preservation of long and continuous records with no erosional hiatuses. The long-term subsidence rate estimated for the investigated sinkhole is 4.2–4.6 mm/yr, whereas average aggradation rates are 2.8–3.1 mm/yr and 2–2.2 mm/yr considering and ignoring the thick detrital units intercalated within the lacustrine facies, respectively. (2) The chronology of the paleoflood deposits

https://doi.org/10.1017/qua.2017.23 Published online by Cambridge University Press

identified in borehole cores can be accurately constrained thanks to the generally high dating potential of the associated lacustrine facies rich in organic remains. In some areas, the success of these investigations may be hindered by the recency of the sinkholes, as well as by high sedimentation rates that overwhelm dissolution-induced subsidence. (3) Oxbow lakes can be used to infer paleoflood histories, as satisfactorily illustrated by Oliva et al. (2016) in the Désert River, southwestern Québec, Canada. However, in the studied reach of the Ebro River valley, most of the lakes related to abandoned meanders date back to the second half of the twentieth century, and consequently, they cannot be used as archives of prehistorical floods, in contrast with the sinkhole ponds that may be older than 2700 yr (Fig. 10). (4) Sinkhole ponds in many regions have been commonly filled by anthropogenic deposits in the last few decades (e.g., Gutiérrez, 2016). These buried depressions, in which drilling is particularly easy, are excellent candidates for paleoflood investigations. (5) Sinkholes may be found in a considerable proportion of fluvial systems worldwide, considering that karst rocks underlie approximately 20% of the earth's continental surface (Ford and Williams, 2007). By extending the temporal length of the flood catalogs with this information, more reliable frequency estimates for high-competence floods could be calculated. Moreover, temporal clusters of paleofloods may be identified and attributed to climatic forcing and/or anthropogenic impacts (e.g., Baker, 2003). Further investigations integrating the information from multiple cores obtained in several sinkhole lakes with variable characteristics and situated in different sectors of the floodplain (Figs. 1 and 3) would help to get deeper insight into the potential of these landforms for paleoflood studies and flood hazard analyses.

The cores derived from sinkhole lakes may also provide practical information on the subsidence phenomenon and may be used for paleoenvironmental investigations. As this study illustrates, quantitative data of interest for sinkhole hazard analysis that may be inferred from the numerically dated successions include: (1) cumulative subsidence magnitude, (2) age of the sinkhole, (3) long-term subsidence rates, and (4) variations in aggradation and subsidence rates through time. A great part of the Holocene paleoenvironmental investigations carried out in the central sector of the Ebro Depression have been focused on playa lakes largely related to wind deflation. These geomorphic settings and the associated stratigraphic records pose important problems, including the presence of long hiatuses related to wind erosion and the scarcity of datable material (e.g., González-Sampériz et al., 2008; Gutiérrez et al., 2013). However, the infill of sinkhole lakes offers continuous and datable records, whose temporal length can be optimized by integrating information from sinkholes of different ages (e.g., floodplain and terraces).

CONCLUSIONS

Sinkhole fills in alluvial systems may be used as archives for paleoflood events. The investigated complex sinkhole illustrates that dissolution-induced subsidence may create two types of geomorphic settings with the potential of preserving stratigraphic records of paleoflood deposits:

1. Benches generated by collapse faulting at the edge of low terraces, where fine-grained slack-water paleoflood deposits may be accumulated. These deposits may have limitations as paleostage indicators for paleodischarge estimation because of two main reasons: (1) they may have been affected by postsedimentary subsidence, and (2) they occur on nonstable valley reaches.
2. Sinkhole ponds located in the floodplain, where the background autochthonous fine-grained sedimentation may be suddenly interrupted by the accumulation of allochthonous coarse-grained deposits during major flood events.

The use of sinkhole ponds as recorders of past floods has a number of advantages: (1) Long-sustained active subsidence contributes to the preservation of continuous stratigraphic successions with no erosional hiatuses. In general, sinkholes related to evaporite dissolution are more favorable because they are typically affected by higher subsidence rates. (2) Generally, paleoflood chronology can be resolved thanks to the high dating potential of the lacustrine facies and the presence of organic remains in the detrital allochthonous facies. (3) The paleoflood investigations should be conducted by integrating data gathered from multiple sinkhole ponds located within the same valley reach, provided precise chronologies are available. The investigations should include sinkholes of different ages, whose aggregate record may cover long paleoflood histories. The selected sinkholes could also be located on variable morphostratigraphic settings (e.g., floodplain, low terraces) where flood deposits may have different sedimentologic signatures and their formation is controlled by variable paleodischarge thresholds.

Nonetheless, they also have significant drawbacks related to the nature of the geomorphic context: (1) paleoflood deposits do not allow inferring paleostage data, although paleocompetence methods could be applied; (2) floods of similar magnitude may produce significantly different sedimentologic signatures because of multiple factors such as the variable distance between the sinkhole and the river channel and the distribution and density of riparian and palustrine vegetation; and (3) the investigation of these deposits, typically located in the subsurface and beneath the water table, need to be investigated via boreholes.

Before using sinkholes for the investigation of past floods, it is highly recommended to characterize the subsidence depressions by integrating data gathered by multiple approaches such as geomorphic mapping, detailed field surveying, shallow geophysics, and trenching.

ACKNOWLEDGMENTS

This work has been funded by project CGL2013-40867-P (Ministerio de Economía y Competitividad, Spain). We are also grateful to Mr. Octavio Plumed from the company ENSAYA for his support for

https://doi.org/10.1017/qua.2017.23 Published online by Cambridge University Press

the borehole drilling. MZ has a position at the Universidad Autónoma de Barcelona as a Serra Hunter Fellow. The work conducted by CC has been supported by project PCIN-2014-106. We thank Kelsey Budahn (Akron University, Ohio) for improving the English of the manuscript.

REFERENCES

Arnaud, A., Adam, N., Hanssen, R., Inglada, J., Duro, J., Closa, J., Eineder, M., 2003. ASAR ERS interferometric phase continuity. 2003 IEEE International Geoscience and Remote Sensing Symposium: Proceedings. IEEE, Piscataway, NJ, pp. 1133–1135.

Baker, V.R., 1987. Paleoflood hydrology and extraordinary flood events. *Journal of Hydrology* 96, 79–99.

Baker, V.R., 2003. Paleofloods and extended discharge records. In Gregory, K.J., Benito, G. (Eds.), *Paleohydrology: Understanding Global Change*. Wiley, Chichester, UK, pp. 307–323.

Baker, V.R., Webb, R.H., House, P.K., 2002. The scientific and societal value of paleoflood hydrology. In House, P.K., Webb, R.H., Baker, V.R., Levish, D.R. (Eds.), *Ancient Floods, Modern Hazards: Principles and Applications of Paleoflood Hydrology. Water Science and Application 5*. American Geophysical Union, Washington, DC, pp. 1–19.

Barreiro-Lostres, F., Moreno, A., Giralt, S., Caballero, M., Valero-Garcés, B., 2014. Climate, palaeohydrology and land use change in the Central Iberian Range over the last 1.6 kyr: the La Parra Lake record. *Holocene* 24, 1177–1192.

Batalla, R.J., Gómez, C.M., Kondolf, G.M., 2004. Reservoir-induced hydrological changes in the Ebro River basin (NE Spain). *Journal of Hydrology* 290, 117–136.

Benito, G., Lang, M., Barriendos, M., Llasat, C., Francés, F., Ouarda, T., Thorndycraft, V.R., *et al*., 2004. Use of systematic, paleoflood and historical data for the improvement of flood risk estimation: review of scientific methods. *Natural Hazards* 31, 623–643.

Benito-Calvo, A., Gutiérrez, F., Carbonel, D., Desir, G., Guerrero, J., Magri, O., Karampaglidis, T., Fabregat, I, 2016. Measuring deformation related to active sinkholes with ground-based 3D laser scanner: a case study in the evaporite karst of the Ebro Valley, NE Spain. In Durán, J.J., Montes, M., Robador, A., Salazar, A. (Eds.), *Comprendiendo el relieve: Del pasado al futuro. XIV Reunión Nacional de Geomorfología, Málaga*. Instituto Geológico y Minero de España, Madrid, pp. 599–606.

Brown, A.L., Reinhardt, E.G., van Hengstum, P.J., Pilarczyk, J.E., 2014. A coastal Yucatan sinkhole records intense hurricane events. *Journal of Coastal Research* 30, 418–428.

Cabezas, A., Comín, F.A., Beguería, S., Trabucchi, M., 2009. Hydrologic and landscape changes in the Middle Ebro River (NE Spain): implications for restoration and management. *Hydrology and Earth System Sciences* 13, 273–284.

Calvo, J.P., Pozo, M., Silva, P.G., Morales, J., 2013. Pattern of sedimentary infilling of fossil mammal traps formed in pseudokarst at Cerro de los Batallones, Madrid Basin, central Spain. *Sedimentology* 60, 1681–1708.

Carbonel, D., Rodríguez, V., Gutiérrez, F., McCalpin, J.P., Linares, R., Roqué, C., Zarroca, M., Guerrero, J., 2014. Evaluation of trenching, ground penetrating radar (GPR) and electrical resistivity tomography (ERT) for sinkhole characterization. *Earth Surface Processes and Landforms* 39, 214–227.

Carbonel, D., Rodríguez-Tribaldos, V., Gutiérrez, F., Galve, J.P., Guerrero, J., Zarroca, M., Roqué, C., Linares, R., McCalpin, J.P., Acosta, E., 2015. Investigating a damaging buried sinkhole cluster in an urban area integrating multiple techniques: geomorphological surveys, DinSAR, GPR, ERT, and trenching. *Geomorphology* 229, 3–16.

Carbonell, E., Bermúdez de Castro, J.M., Parés, J.M., Pérez-González, A., Cuenca-Bescos, G., Ollé, A., Mosquera, M., *et al*., 2008. The first hominid of Europe. *Nature* 452, 465–469.

Castañeda, C., Gutiérrez, F., Manunta, M., Galve, J.P., 2009. DInSAR measurements of ground deformation by sinkholes, mining subsidence, and landslides, Ebro River, Spain. *Earth Surface Processes and Landforms* 34, 1562–1574.

Confederación Hidrográfica del Ebro (CHEbro). 2015. *Informe sobre las avenidas del primer trimestre de 2015 en la Cuenca del Ebro*. CHEbro, Zaragoza, Spain. http://www.chebro.es/contenido.streamFichero.do?idBinario=19259.

Comisión Nacional de Protección Civil (CNPC). 1985. *Estudio de inundaciones históricas. Mapa de riesgos potenciales. Cuenca del Ebro. Comisión Técnica de Inundaciones*. Gobierno de España, Madrid.

Crosetto, M., Biescas, E., Duro, J., Closa, J., Arnaud, A., 2008. Generation of advanced ERS and Envisat interferometric SAR products using the Stable Point Network technique. *Photogrammetric Engineering and Remote Sensing* 74, 443–450.

Dahlin, T., Zhou, B., 2004. A numerical comparison of 2D resistivity imaging with 10 electrode arrays. *Geophysical Prospecting* 52, 379–398.

Desir, G., Guerrero, J., Gutiérrez, F., Carbonel, D., Merino, J., Benito, A., Fabregat, I., Roqué, C., Zarroca, M., Linares, R., 2016. Monitorización de dolinas activas en el entorno de Zaragoza mediante nivelación geométrica de alta precisión. In Durán, J.J., Montes, M., Robador, A., Salazar, A. (Eds.), *Comprendiendo el relieve: Del pasado al futuro. XIV Reunión Nacional de Geomorfología, Málaga*. Instituto Geológico y Minero de España, Madrid, pp. 607–613.

Espejo, F., Domenech, S.M., Ollero, A., Sanchez, M., 2008. La crecida del Ebro de 2007: Procesos hidrometeorológicos y perspectivas de gestión del riesgo. *Boletín de la Asociación de Geógrafos Españoles* 48, 129–154.

Ford, D.C., Williams, P., 2007. *Karst Hydrogeology and Geomorphology*. Wiley, Chichester, UK.

Galve, J.P., Castañeda, C., Gutiérrez, F., 2015. Railway deformation detected by DInSAR over active sinkholes in the Ebro Valley evaporite karst, Spain. *Natural Hazards and Earth System Science* 3, 3967–3981.

Galve, J.P., Gutiérrez, F., Lucha, P., Bonachea, J., Cendrero, A., Gimeno, M.J., Gutiérrez, M., Pardo, G., Remondo, J., Sánchez, J.A., 2009. Sinkholes in the salt-bearing evaporite karst of the Ebro River valley upstream of Zaragoza city (NE Spain): geomorphological mapping and analysis as a basis for risk management. *Geomorphology* 108, 145–158.

Gischler, E., Shinn, E.A., Oschmann, W., Fiebig, J., Buter, N.A., 2008. A 1500-yr Holocene Caribbean climate archive from the Blue Hole, Lighthouse Reef, Belize. *Journal of Coastal Research* 24, 1495–1505.

González-Sampériz, P., Valero-Garcés, B.L., Moreno, A., Morellón, M., Navas, A., Machín, J., Delgado-Huertas, A., 2008. Vegetation changes and hydrological fluctuations in the Central Ebro Basin (NE Spain) since the Late Glacial period: saline lake records. *Paleogeography, Paleoclimatology, Paleoecology* 259, 157–181.

Griffiths, D.H., Barker, R.D., 1993. Two-dimensional resistivity imaging and modelling in areas of complex geology. *Journal of Applied Geophysics* 29, 211–226.

Guerrero, J., Gutiérrez, F., Galve, J.P., 2013. Large depressions, thickened terraces, and gravitational deformation in the Ebro River valley (Zaragoza area, NE Spain): evidence of glauberite and halite interstratal karstification. *Geomorphology* 196, 162–176.

Gutiérrez, F., 2016. Sinkhole hazards. In Cutter, S.L. (Ed.), *Oxford Research Encyclopedia of Natural Hazard Science*. Oxford University Press, Oxford, pp. 1–88. http://naturalhazardscience.oxfordre.com/view/10.1093/acrefore/9780199389407.001.0001/acrefore-9780199389407-e-40?print=pdf.

Gutiérrez, F., Cooper, A.H., 2013. Surface morphology of gypsum karst. In Frumkin, A. (Ed.), *Treatise on Geomorphology* Vol. 6, Karst Geomorphology. Elsevier, Amsterdam, pp. 425–437.

Gutiérrez, F., Fabregat, I., Roqué, C., Carbonel, D., Guerrero, J., García-Hermoso, F., Zarroca, M., Linares, R., 2016. Sinkholes and caves related to evaporite dissolution in a stratigraphically and structurally complex setting, Fluvia Valley, eastern Spanish Pyrenees. Geological, geomorphological and environmental implications. *Geomorphology* 267, 76–97.

Gutiérrez, F., Galve, J.P., Guerrero, J., Lucha, P., Cendrero, A., Remondo, J., Bonachea, J., Gutiérrez, M., Sánchez, J.A., 2007. Typology, spatial distribution and detrimental effects of the sinkholes developed in the alluvial evaporite karst of the Ebro River valley downstream Zaragoza city. *Earth Surface Processes and Landforms* 32, 912–928.

Gutiérrez, F., Galve, J.P., Lucha, P., Bonachea, J., Jordá, L., Jordá, R., 2009. Investigation of a large collapse sinkhole affecting a multi-storey building by means of geophysics and the trenching technique, Zaragoza city, NE Spain. *Environmental Geology* 58, 1107–1122.

Gutiérrez, F., Galve, J.P., Lucha, P., Castañeda, C., Bonachea, J., Guerrero, J., 2011. Integrating geomorphological mapping, trenching, InSAR and GPR for the identification and characterization of sinkholes in the mantled evaporite karst of the Ebro Valley (NE Spain). *Geomorphology* 134, 144–156.

Gutiérrez, F., Guerrero, J., Lucha, P., 2008. A genetic classification of sinkholes illustrated from evaporite paleokarst exposures in Spain. *Environmental Geology* 53, 993–1006.

Gutiérrez, F., Mozafari, M., Carbonel, D., Gómez, R., Raeisi, E., 2015. Leakage problems in dams built on evaporites. The case of La Loteta Dam (NE Spain), a reservoir in a large karstic depression generated by interstratal salt dissolution. *Engineering Geology* 185, 139–154.

Gutiérrez, F., Parise, M., De Waele, J., Jourde, H., 2014. A review on natural and human induced geohazards and imapcts in karst. *Earth Science Reviews* 138, 61–88.

Gutiérrez, F., Valero-Garcés, B., Desir, G., González-Sampériz, P., Gutiérrez, M., Linares, R., Zarroca, M., *et al*., 2013. Late Holocene evolution of playa lakes in the central sector of the Ebro Depression based on geophysical surveys and morpho-stratigraphic analysis of lacustrine terraces. *Geomorphology* 196, 177–197.

Hart, E.A., 2014. Legacy sediment stored in sinkholes: a case study of three urban watersheds in Tennessee, United States of America. *Physical Geography* 35, 514–531.

Henderson, F.M., Lewis, A.J., 1998. *Manual of Remote Sensing: Principles and Applications of Imaging Radars*. John Wiley and Sons, New York.

Hyatt, J.A., Gilbert, R., 2004. Subbottom acoustic and sedimentary records of past surface water-groundwater exchange through sinkhole lakes in south Georgia, USA. *Environmental Geology* 46, 32–46.

Kochel, R.C., Baker, V.R., 1982. Paleoflood hydrology. *Science* 215, 353–361.

Kochel, R.C., Baker, V.R., 1988. Paleoflood analysis using slackwater deposits. In Baker, V.R., Kochel, R.C., Patton, P.C. (Eds.), *Flood Geomorphology*. Wiley, New York, pp. 357–402.

Lane, P., Donnelly, J.P., Woodruff, J.D., Hawkes, A.D., 2011. A decadally-resolved paleohurricane record archived in the late Holocene sediments of a Florida sinkhole. *Marine Geology* 287, 14–30.

Langer, H., Offermann, H., 1982. On the solubility of sodium chloride in water. *Journal of Crystal Growth* 60, 389–392.

Laury, R.L., 1980. Paleoenvironment of a late Quaternary mammoth-bearing sinkhole deposit, Hot Springs, South Dakota. *Geological Society of America Bulletin* 91, 465–475.

Loke, M.H., Barker, R.D., 1996. Rapid least-squares inversion of apparent resistivity pseudosections by a quasi-Newton method. *Geophysical Prospecting* 44, 131–152.

Loke, M.H., Chambers, J.E., Rucker, D.F., Kuras, O., Wilkinson, P. B., 2013. Recent developments in the direct-current geoelectrical imaging method. *Journal of Applied Geophysics* 95, 135–156.

López-Moreno, J.I., Beguería, S., García-Ruiz, J.M., 2002. Influence of the Yesa reservoir on floods of the Aragón River, central Spanish Pyrenees. *Hydrology and Earth System Sciences* 6, 753–762.

Losada, J.A., Montesinos, S., Omedas, M., García-Vera, M.A., Galván, R., 2004. Cartografía de las inundaciones del río Ebro en febrero de 2003: trabajos de fotointerpretación, teledetección y análisis SIG en el GIS-Ebro. In Conesa, C., Álvarez, Y., Martínez, J.B. (Eds.), *Medio ambiente, recursos y riesgos naturales: análisis mediante tecnología SIG y teledetección*. Vol. 2. Asociación de Geógrafos Españoles–Universidad de Murcia, Murcia, Spain, pp. 207–218.

Magdaleno, F., Fernández-Yuste, J.A., 2011. Meander dynamics in a changing corridor. *Geomorphology* 130, 197–207.

Maiziels, J.K., 1983. Paleovelocity and paleodischarge determination for coarse gravel deposits. In Gregory, K.J. (Ed.), *Background to Paleohydrology*. Wiley, Chichester, UK, pp. 101–139.

McCalpin, J.P., 2009a. Field techniques in paleoseismology—terrestrial environments. In McCalpin, J.P. (Ed), *Paleoseismology*. Academic Press, San Diego, CA, pp. 29–118.

McCalpin, J.P., 2009b. Paleoseismology in extensional tectonic environments. In McCalpin, J.P. (Ed.), *Paleoseismology*. Academic Press, San Diego, CA, pp. 171–269.

Mejón, M., 2011. *El Ebro desbordado*. Ayuntamiento de Zaragoza, Zaragoza, Spain.

Morellón, M., Valero-Garcés, B., Anselmetti, F., Ariztegui, D., Schnellmann, M., Moreno, A.N.A., Mata, P., Rico, M., Corella, J.P., 2009. Late Quaternary deposition and facies model for karstic Lake Estanya (North-eastern Spain). *Sedimentology* 56, 1505–1534.

Oliva, F., Viau, A.E., Bjornson, J., Desrochers, N., Bonneau, M.-A., 2016. A 1300 year reconstruction of paleofloods using oxbow lake sediments in temperate southwestern Québec, Canada. *Canadian Journal of Earth Sciences* 53, 378–386.

Ollero, A., 1995. Dinámica reciente del cauce del Ebro en la Reserva Natural de los Galachos (Zaragoza). *Cuaternario y Geomorfología* 9, 85–93.

Ollero, A., 2010. Channel changes and floodplain management in the meandering middle Ebro River, Spain. *Geomorphology* 117, 247–260.

https://doi.org/10.1017/qua.2017.23 Published online by Cambridge University Press

Ortí, F., Salvany, J.M., 1997. Continental evaporitic sedimentation in the Ebro Basin during the Miocene. In Busson, G., Schreiber, B.C. (Eds.), *Sedimentary Deposition in Rift and Foreland Basins in France and Spain*. Columbia University Press, New York, pp. 420–429.

Quirantes, J., 1978. *Estudio sedimentológico y estratigráfico del Terciario continental de los Monegros*. Institución Fernando el Católico (CSIC), Zaragoza, Spain.

Regato, P., 1988. *Contribución al estudio de la flora y la vegetación del "Galacho de La Alfranca" en relación con la evolución del sistema fluvial*. Diputación General de Aragón, Zaragoza, Spain.

Reimer, P.J., Bard, E., Bayliss, A., Beck, J.W., Blackwell, P.G., Bronk Ramsey, C., Grootes, P.M., *et al*., 2013. IntCal13 and Marine13 radiocarbon age calibration curves 0–50,000 years cal BP. *Radiocarbon* 55, 1869–1887.

Salvany, J.M., 2009. *Geología del yacimiento glauberítico de Montes de Torrero*. Universidad de Zaragoza, Zaragoza, Spain.

Salvany, J.M., García-Veigas, J., Ortí, F., 2007. Glauberite–halite association of the Zaragoza Gypsum Formation (Lower Miocene, Ebro Basin, NE Spain). *Sedimentology* 54, 443–467.

Sheffer, N.A., Enzel, Y., Benito, G., Grodek, T., Poart, N., Lang, M., Coeur, D., 2003. Paleofloods and historical floods of the Ardèche River, France. *Water Resources Research* 39, 1376. http://dx.doi.org/10.1029/2003WR002468.

Simón Gómez, J.L., Soriano Jiménez, M.A., Arlegui Crespo, L., Caballero Burbano, J., 1998. *Estudio de riesgos de hundimientos kársticos en el corredor de la carretera de Logroño. Memoria del Plan General de Ordenación Urbana de Zaragoza (P.G.O.U.Z.), Anejo 3.2*. Departamento de Geología, Universidad de Zaragoza, Zaragoza, Spain. http://www.zaragoza.es/contenidos/urbanismo/pgouz/memoria/anejos/anejo03/anejo032.pdf.

Thorndycraft, V.R., Benito, G., 2006. The Holocene fluvial chronology of Spain: evidence from a newly compiled radiocarbon database. *Quaternary Science Reviews* 25, 223–234.

Torrescusa, S., Klimowitz, J., 1990. Contribución al conocimiento de las evaporitas Miocenas (Formación Zaragoza) de la Cuenca del Ebro. In Ortí, F., Salvany, J.M. (Eds.), *Formaciones evaporíticas de la Cuenca del Ebro y cadenas periféricas y de la zona de Levante*. ENRESA-GPG, Barcelona, Spain, pp. 120–122.

Turnage, K.M., Lee, S.Y., Foss, J.E., Kim, K.H., Larsen, I.L., 1997. Comparison of soil erosion and deposition rates using radiocesium, RUSLE, and buried soils in dolines in East Tennessee. *Environmental Geology* 29, 1–10.

Webb, R.H., Blainey, J.B., Hyndman, D.W., 2002. Paleoflood hydrology of the Paria River, southern Utah and northern Arizona, USA. In House, P.K., Webb, R.H., Baker, V.R., Levish, D.R. (Eds.), *Ancient Floods, Modern Hazards: Principles and Applications of Paleoflood Hydrology. Water Science and Application 5*. American Geophysical Union, Washington, DC, pp. 295–310.

Whitmore, T.J., Brenner, M., Curtis, J.H., Dahlin, B.H., Leyden, B. W., 1996. Holocene climatic and human influences on lakes of the Yucatan Peninsula, Mexico: an interdisciplinary, palaeolimnological approach. *Holocene* 6, 273–287.

Williams, G.P., 1984. Paleohydrological equations for rivers. In Costa, J.E., Fleisher, P.J. (Eds.), *Developments and Applications of Geomorphology*. Springer-Verlag, Berlin, pp. 343–367.

Zaidner, Y., Frumkin, A., Porat, N., Tsatskin, A., Yeshurun, R., Weissbrod, L., 2014. A series of Mousterian occupations in a new type of site: the Nesher Ramla karst depression, Israel. *Journal of Human Evolution* 66, 1–17.

Zarroca, M., Comas, X., Gutiérrez, F., Carbonel, D., Linares, R., Roqué, C., Mozaffari, M., Guerrero, J., Pellicer, X.M., 2016. The application of GPR and ERI in combination with exposure logging and retrodeformation analysis to characterize sinkholes and reconstruct their impact on fluvial sedimentation. Earth Surface Processes and Landforms (in press). http://dx.doi.org/10.1002/esp.4069.

https://doi.org/10.1017/qua.2017.23 Published online by Cambridge University Press